



Tuning excited-state electronic structure in tungsten oxide for enhanced nitrogen photooxidation as fertilizer

Shaoquan Li^{a,1}, Jinjia Liu^{c,f,1}, Wenli Su^d, Yi Wang^a, Jinhao Li^a, Chenjun Ning^a, Jing Ren^a, Xiaodong Wen^c, Wenkai Zhang^d, Yuxin Tong^e, Chong Wang^e, Lirong Zheng^g, Wei Zhang^h, Dermot O'Hareⁱ, Yufei Zhao^{a,b,*}, Xue Duan^{a,b}

^a State Key Laboratory of Chemical Resource Engineering, Beijing University of Chemical Technology, Beijing 100029, PR China

^b Quzhou Institute for Innovation in Resource Chemical Engineering, Quzhou, Zhejiang, PR China

^c State Key Laboratory of Coal Conversion, Institute of Coal Chemistry, Chinese Academy of Sciences, Taiyuan 030001, PR China

^d Department of Physics and Applied Optics Beijing Area Major Laboratory, Center for Advanced Quantum Studies, Beijing Normal University, Beijing 100875, PR China

^e Institute of Environment and Sustainable Development in Agriculture, Chinese Academy of Agricultural Sciences, Beijing 100081, PR China

^f National Energy Center for Coal to Clean Fuels, Synfuels China Co., Ltd, Huairou District, Beijing 101400, PR China

^g Beijing Synchrotron Radiation Facility, Institute of High Energy Physics, Chinese Academy of Sciences, Beijing 100049, PR China

^h Chongqing Institute of Green and Intelligent Technology, Chinese Academy of Sciences, Chongqing 400714, PR China

ⁱ Chemistry Research Laboratory, Department of Chemistry, University of Oxford, Mansfield Road, Oxford OX1 3TA, United Kingdom

ARTICLE INFO

Keywords:

Photocatalytic nitrogen fixation
Electronic structure regulation
Tungsten oxide
Solar N-fertilizer

ABSTRACT

Nitrate (NO_3^-) is an important raw ingredient for fertilizer, but its conventional synthesis is restricted by high energy consumption and CO_2 emissions. Though there have been some studies on photocatalytic nitrogen oxidation, the production rate of nitrate is undesirable and the excited-state charge-transfer pathway still remains unclear. Herein, we fabricated the V-doped $\text{W}_{18}\text{O}_{49}$ nanowires (V- $\text{W}_{18}\text{O}_{49}$) for direct nitrate synthesis from N_2 photooxidation. The NO_3^- production rate is as high as $39.85 \mu\text{mol g}^{-1} \text{h}^{-1}$ with exceptional catalytic stability and the photosynthetic nitrate fertilizer was employed to promote the growth of crops. Time-resolved spectroscopic results confirmed that the introduction of V doping in V- $\text{W}_{18}\text{O}_{49}$ has created new high-efficiency electron-transfer (ET) pathways from the W-O site to the V-dopant under photoirradiation, which leads to an improved π -backdonation process that facilitates nitrogen activation. This newly formed ET channel facilitated efficient charge separation and ultrafast photogenerated carriers transfer, thus overcame the sluggish ET kinetics.

1. Introduction

Nitrate is an indispensable commodity in agriculture and the chemical industry [1]. Nowadays, nitrate is produced by the tandem of both the Haber-Bosch and Ostwald processes. However, these centralized processes are highly energy consuming, require significant amounts of H_2 , and release vast quantities of CO_2 [2]. Recently, the utilization of clean energy to facilitate the efficient direct N_2 fixation to N-fertilizer has attracted widespread attention in the scientific community [3,4]. Recent research has revealed that the nitrate can be formed from atmospheric N_2 and O_2 under UV or sunlight irradiation [5]. Nevertheless, the difficult $\text{N}\equiv\text{N}$ bond dissociation and rapid electron-hole

recombination led to diminished N_2 oxidation reaction (NOR) performance [5]. Therefore, the rational design of highly efficient photocatalysts toward N_2 fixation into NO_3^- as "solar fertilizer" is an urgent requirement.

Excited-state charge transfer process is vital important in photocatalytic NOR as they limit the N_2 activation efficiency. As a result, clarifying the excited-state electronic structure and charge-transfer can help recognize the origin of limitations of N_2 conversion efficiency and improve the photocatalytic nitrogen oxidation performance. In general, heteroatom doping [6,7] could modulate the electronic states of photocatalysts to promote the charge transfer process in N_2 activation. And as an important kind of tungsten oxide compound, the

* Corresponding author at: State Key Laboratory of Chemical Resource Engineering, Beijing University of Chemical Technology, Beijing 100029, PR China
E-mail address: zhaoyufei@mail.buct.edu.cn (Y. Zhao).

¹ These authors contributed equally to this work.

nonstoichiometric tungsten oxide $W_{18}O_{49}$ with abundant oxygen vacancies has gained great attention in photocatalysis [8,9]. Xiong *et al.* demonstrated that Mo-doped $W_{18}O_{49}$ nanowires could enhance the yield of ammonia [10]. Bi *et al.* fabricated Fe-doped $W_{18}O_{49}$ nanowires with the surface anchoring of black phosphorus quantum dots (BPQDs), which significantly promoted the photocatalytic N_2 fixation [11]. Even though numerous efforts have been made [3,12–15], it remains an enduring challenge to regulate the intermediate adsorption and activation in NOR as the transition metals have different electron structures. More importantly, the excited-state electronic structure and charge-transfer process in photocatalytic NOR are not well unraveled. Thus, it is of great practical value to design a robust photocatalyst and reveal the excited-state electronic structure in N_2 -to- NO_3^- conversion.

In this study, we have developed the V-doped $W_{18}O_{49}$ nanowires (referred to as V- $W_{18}O_{49}$) for nitrate synthesis from N_2 . Under light irradiation, the production rate of nitrate is as high as $39.85 \mu\text{mol g}^{-1} \text{h}^{-1}$. In the liquid phase, the product of nitrogen fixation is nitrate, which can be utilized directly as a N-fertilizer for enhanced Cole crop growth. Our study reveals that the doping of V in $W_{18}O_{49}$ effectively modulates the electronic states of $W_{18}O_{49}$, leading to the emergence of an extra electron-transfer (ET) pathway from the W-O site to V-dopant. This newly formed ET channel exhibits a prolonged decay time upon irradiation, thereby mitigating the issue of excessive O_2 adsorption and improving the sluggish ET kinetics. The theoretical calculations, additionally suggest that the introduction of V doping had a regulatory effect on the local electron states and facilitated the π -backdonation process during the N_2 activation. Our work provides a promising avenue toward value-added nitrate synthesis by constructing the electronic structure of photocatalyst and develop the potential applications in agriculture.

2. Experimental and computational section

2.1. Catalyst synthesis and morphology

The V- $W_{18}O_{49}$ nanowires were synthesized by a mild solvothermal method. In a typical synthesis process, 100 mg of WCl_6 was dissolved into 69 mL of absolute ethanol with vigorously stirring for 30 min. Then 1 mL of ethanol solution containing different amounts of VCl_3 was added into the obtained yellow solution, which was further stirred for 10 min and transferred into a 100 mL Teflon-lined stainless-steel autoclave, and subsequently thermally treated at 200°C for 12 h. The dark blue product was centrifuged and washed with absolute ethanol and water multiple times. Finally, the product was dried in vacuum at 25°C overnight. The pure $W_{18}O_{49}$ nanowires were synthesized by the same method without adding VCl_3 .

2.2. Photocatalytic N_2 oxidation tests

The photocatalytic N_2 oxidation tests were conducted in a home-made quartz reaction chamber which was operated as a flow reactor with a top quartz window for light irradiation. 5 mg catalysts were uniformly dispersed as a thin layer in the reaction chamber. Subsequently, a dry simulated air ($N_2: O_2 = 4:1$) was introduced into the reactor, with the gas flow rate of 200 mL min^{-1} continuously at room temperature. A 300 W Xenon lamp (Beijing Perfect-light Co. Ltd, PLS-SXE-300UV) was used as the light source. A 300 W Xenon lamp with an AM 1.5 G filter was employed to imitate solar light, and light intensity was measured to be 100 mW cm^{-2} (1 sun). Gas scrubbers were used to collect products. After the reaction finished, we continued to purge with reaction gas for 20 min and the catalysts were washed with ultrapure water to collect part of the products. The concentrations of HNO_3 were quantified by ion chromatography (ICS-1000, Thermo Fisher). The gas was detected through the NOx analyzer (Thermo Scientific 42i).

The yield of NO_3^- was calculated through the following equation:

$$y(NO_3^-) = \frac{C(NO_3^-) * V}{n(NO_3^-) * m_{(Cat.)} * t}$$

where $C_{(NO_3^-)}$ represent the NO_3^- concentration detected by ion chromatography (IC); V represent the volume of water in the gas scrubbers; $n_{(NO_3^-)}$ is the relative molecular mass; $m_{(cat.)}$, t are the catalyst dosage and reaction time, respectively.

2.3. The density functional theory (DFT) calculation

All spin-polarization calculations were carried out with plane-wave-based DFT method in the Vienna Ab initio Simulation Package (VASP) [16]. The calculations were based on a plane-wave density functional theory (DFT) approach with the Perdew-Burke-Ernzerh of functional of generalized gradient approximation (GGA-PBE) used to describe exchange and correction interaction [17,18]. The electron-ion interaction was described using projector-augmented wave (PAW) potentials [19]. A plane-wave cutoff energy of 400 eV was applied, and the calculations were carried out until the forces in each degree of freedom and energy difference reached the limit of 0.02 eV/\AA and 10^{-4} eV , respectively. The excited-state calculations were obtained using constrained DFT [20], where one electron was promoted from the highest occupied molecular orbitals to the lowest unoccupied molecular orbitals at each k point. The adsorption energy was calculated using Eq. (1), which considers the total energy of the slab with adsorbates in its equilibrium geometry ($E_{x/slab}$), the total energy of the bare slab (E_{slab}), and the total energy of the free adsorbates in the gas phase (E_x). The $W_{18}O_{49}(010)$ slab model was used to represent the $W_{18}O_{49}$ catalysts, with 54 W and 129 O atoms. For the V- $W_{18}O_{49}(010)$ model, two surface W atoms were replaced by V atoms. A 15 \AA vacuum layer was used for all slab models. During the calculations, 18 W and 49 O atoms were fixed, while the other atoms were allowed to relax. The Gamma point was used for all calculations.

$$E_{ads} = E_{x/slab} - E_x - E_{slab} \quad (1)$$

2.4. The time-dependent DFT (TDDFT) calculation

The software used in the TDDFT calculation part of this work is CP2K version 9.0, which can calculate the excited state electronic structure of the larger periodic system [21]. The chosen K-point is Gamma, utilizing the GTH-PBE potential and the DZVP-MOLOPT-SR-GTH basis set. The cutoff energy is specified as 350 eV, while EPS_SCF has been established at $5.0E-06$ to ensure convergence of the density matrix during SCF. ADDED_MOS has been set at 1000. In order to conduct a thorough analysis of higher-order excited states, it is advisable to compute additional empty orbitals for hole-electron calculation, as the configuration function involving these orbitals is often overlooked. A total of 3000 excited states are calculated with a MIN_AMPLITUDE of 0.01, representing the lowest acceptable level of excitation amplitude for printing. Due to the large periodicity of the system, which consumes computational resources and is time-consuming, this work requires approximately 560 cores to run properly.

The drawing of differential charge density diagram of specific excited state is analyzed by combining the output file obtained by TDDFT with Multiwfn software (2023-Feb-10 and later updated versions of Multiwfn can realize this function). Hole-electron analysis is a very powerful and practical method to investigate the characteristics of electron excitation supported by the Multiwfn program. It describes the process of electron excitation as "hole \rightarrow electron", so that we can visually investigate where the electron leaves and goes, whether it is local excitation, global excitation, electron transfer excitation or hybrid excitation.

3. Results and discussion

3.1. Catalyst synthesis and morphology

Pristine $W_{18}O_{49}$ nanowires were first obtained through a facile solvothermal method [22], and then the V doped $W_{18}O_{49}$ nanowires by the same method were carried out using the same solvothermal method (Fig. 1a, Fig. S1, see Methods). The catalysts were synthesized in the absence of any N-containing compounds. The powder X-ray diffraction (XRD) data for $W_{18}O_{49}$ and V- $W_{18}O_{49}$ were recorded, characteristic peaks at $2\theta = 23.4^\circ$ and 47.8° can be indexed to the (010) and (020) Bragg reflections respectively of monoclinic $W_{18}O_{49}$ (JCPDS card No. 71–2450, Fig. S2), indicating the successfully synthesis of the tungsten oxide. And the (010) peak of the V- $W_{18}O_{49}$ shifted 0.06° after V doping, which can be attributed to the slight contraction of the monoclinic structure of $W_{18}O_{49}$ due to the V-doping [23]. Moreover, the transmission electron microscopy (TEM) and scanning transmission electron microscopy (STEM) images indicated an obvious one-dimensional morphology for both $W_{18}O_{49}$ (Fig. 1b) and V- $W_{18}O_{49}$ (Fig. 1d, Fig. S3) with an average diameter of 3–5 nm. A high resolution TEM (HRTEM) images show lattice fringes with an interplanar distance of 3.8 Å, which

can be attributed to the (010) plane of monoclinic $W_{18}O_{49}$ (Fig. 1c and Fig. 1e). Above results demonstrate that the monoclinic phase of $W_{18}O_{49}$ remains after V doping. Furthermore, both high-angle annular darkfield STEM (HAADF-STEM) image and the EDX elemental mapping images revealed a uniform dispersion of V throughout the length of the $W_{18}O_{49}$ nanowires (Fig. 1f–g).

3.2. Photocatalytic NOR performance

The performance of the as-obtained V- $W_{18}O_{49}$ sample for photocatalytic N_2 oxidation reaction (NOR) was evaluated. The photocatalytic experiments were performed in simulated air ($N_2:O_2 = 4:1$) under UV–vis light irradiation in a gas-flowing tandem system. In this reaction system, the produced nitrate (HNO_3) was detected by the ion chromatograph method (Fig. S4) and the gas N-contained product was detected by the NO_x analyzer (Fig. S5). The effect of doping amounts of V component in $W_{18}O_{49}$ was first studied, and the V-doping $W_{18}O_{49}$ structure with a V loading amount of 3.75 mol% had the best NOR performance with a remarkable NO_3^- production rate of $39.85 \text{ mol g}^{-1} \text{ h}^{-1}$ (Fig. S6, Supplementary Table 1, Fig. 2a and Fig. S7). It is worth noting that the NOR performance of $W_{18}O_{49}$ without V doping was

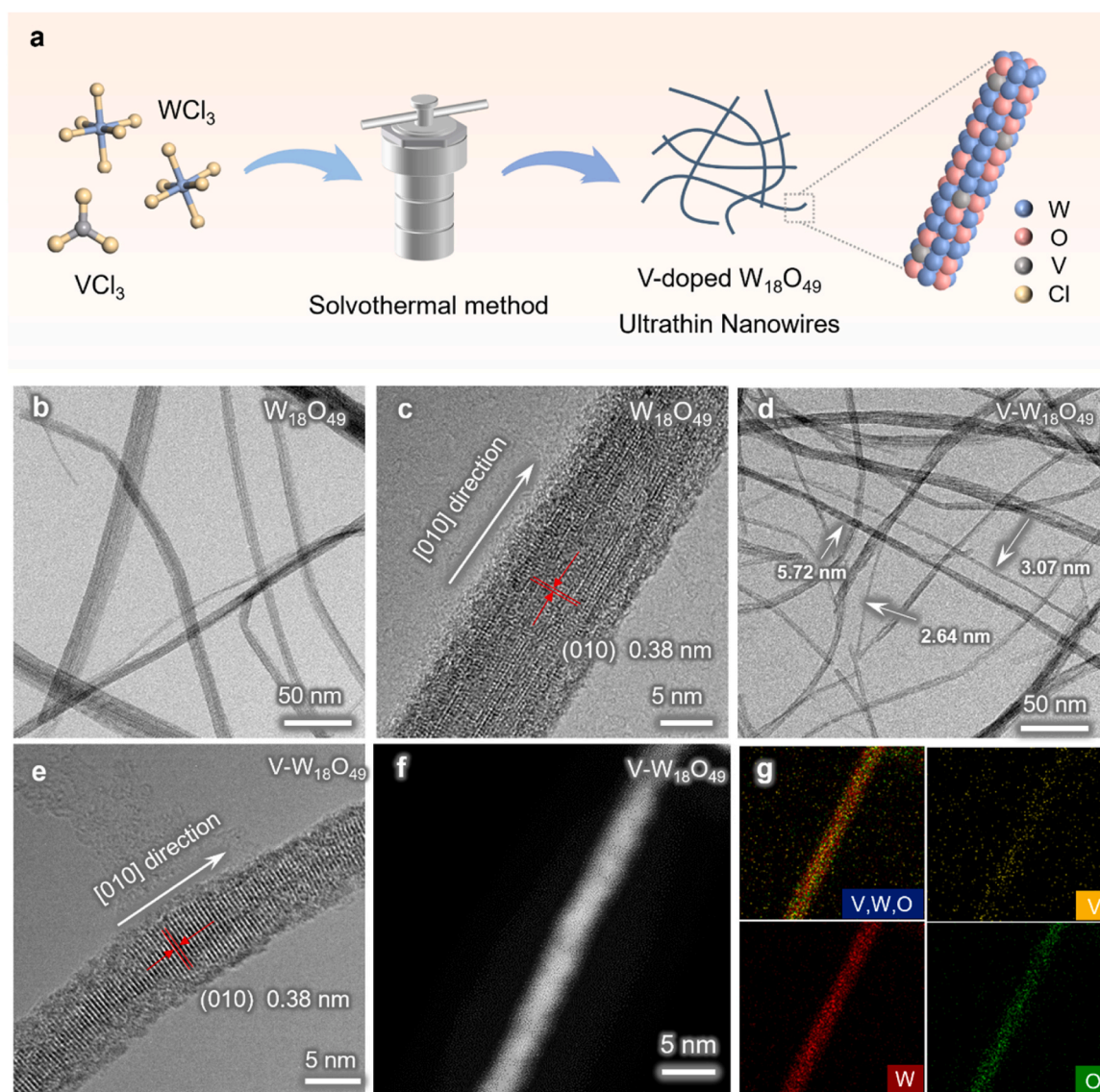


Fig. 1. Characterizations of V- $W_{18}O_{49}$ nanowires. (a) The schematic illustration for the synthesis of V- $W_{18}O_{49}$. (b) TEM and (c) HRTEM images of $W_{18}O_{49}$. (d) TEM and (e) HRTEM images of V- $W_{18}O_{49}$. (f) HAADF-STEM image of V- $W_{18}O_{49}$ and (g) the corresponding elemental mapping images of V, W and O.

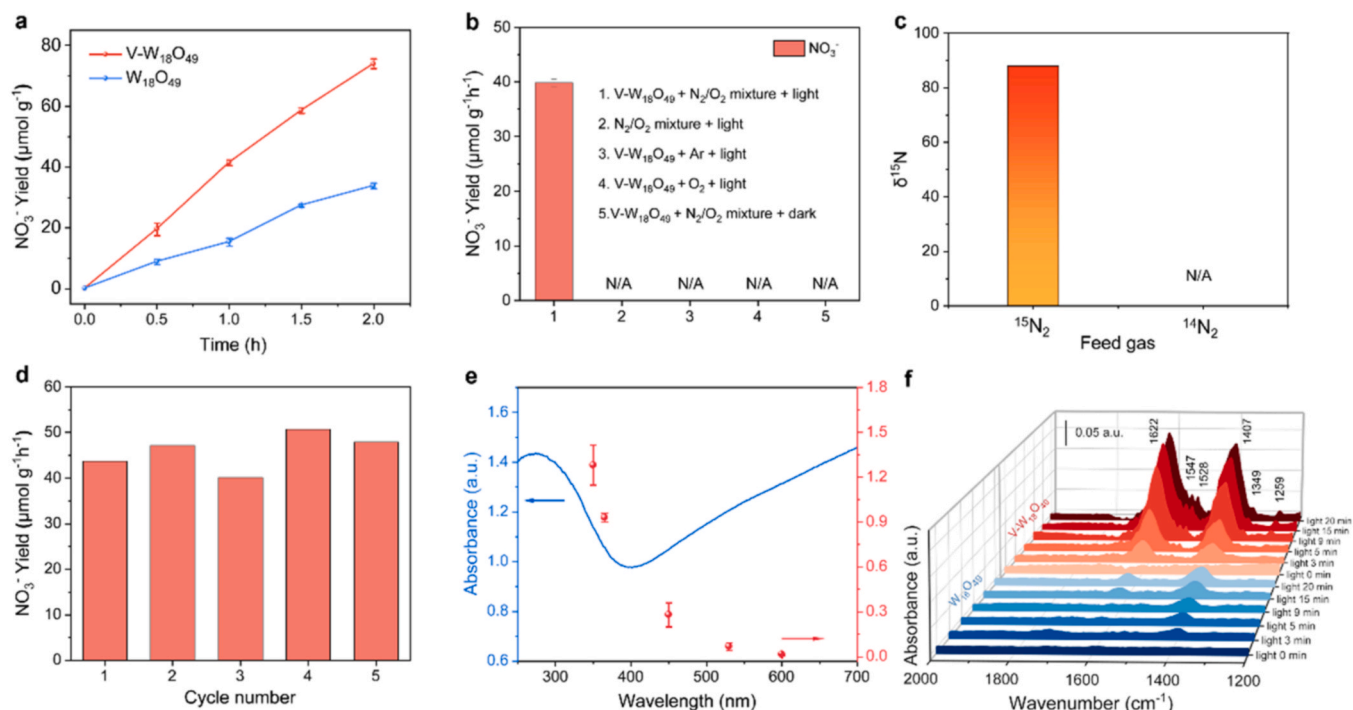


Fig. 2. (a) Time-dependent HNO₃ production rate for V-W₁₈O₄₉. (b) HNO₃ yield rate under different conditions (“N/A” denotes “not detected”). (c) The testing concentration of ¹⁵N Isotope Ratio Mass Spectrometer. (d) Cycle tests for photocatalytic HNO₃ synthesis over V-W₁₈O₄₉ (1 h for a cycle). (e) Calculated AQEs for N₂ oxidation over V-W₁₈O₄₉. (f) The in-situ DRIFTS over V-W₁₈O₄₉ and W₁₈O₄₉.

rather poor that only gave a HNO₃ production rate of 17.04 μmol g⁻¹ h⁻¹. The NOR performance of V-W₁₈O₄₉ exceeds most currently known catalysts systems (Supplementary Table 3).

Control experiments have shown that the N₂/O₂ atmosphere, light irradiation, and photocatalysts are all necessary to initiate oxidation of N₂ (Fig. 2b). To further confirm that the nitrate products were generated from the N₂ oxidation, ¹⁵N/¹⁴N isotope labeling experiments were carried out. ¹⁵NO₃⁻ was detected by stable isotope-ratio mass spectrometry [24]. The parameter δ¹⁵N (δ¹⁵N = R(¹⁵N/¹⁴N_{sample})/R(¹⁵N/¹⁴N_{air}) - 1) was adopted to evaluate the ¹⁵N concentration in ¹⁵NO₃⁻ products in Fig. 2c. When ¹⁴N₂ was used as feed gas, the detected N isotope was exclusively ¹⁴N with no ¹⁵N present. When ¹⁵N₂ (>98 atom % ¹⁵N) was pumped into the reactor, the δ¹⁵N value was much more than the corresponding standard abundance. These findings confirm that atmospheric N₂ was the source of nitrogen in the photocatalytic nitrate product.

To further examine the catalytic stability of the V-W₁₈O₄₉ nanowires, the V-W₁₈O₄₉ sample were collected for cycling tests (Fig. 2d). The rate of NO₃⁻ production rate of over 39.5 μmol g⁻¹ h⁻¹ was maintained throughout the recycle tests, illustrating the superior stability of V-W₁₈O₄₉. The XRD and XAFS data for V-W₁₈O₄₉ after five catalytic cycles exhibited no obvious changes, the HRTEM images confirmed the stability of the monoclinic structure of V-W₁₈O₄₉ by comparison with the fresh sample (Fig. S8 and 9), this suggests excellent structural stability and reusability of V-W₁₈O₄₉ for direct photocatalytic nitrogen oxidation. To explore the relationships between irradiation wavelength and nitrate production, the apparent quantum efficiency (AQE) was evaluated under monochromatic irradiation (Fig. 2e). We observed a decline in AQE from 1.28 % to 0.01 % when the wavelength was increased from 350 to 600 nm, this is in agreement with the absorption spectrum of V-W₁₈O₄₉.

In order to probe intermediate species during the photocatalytic N₂ oxidation process, we employed in-situ diffuse reflectance infrared Fourier-transform spectroscopy (in-situ DRIFTS). As shown in Fig. 2f, no species were found in atmospheric N₂ and O₂ before irradiation. Upon

light irradiation, several absorption features appeared and gradually increased in intensity as a function of reaction time. The absorption features at 1622 cm⁻¹ can be ascribed to the stretching vibrational of an *O₂N₂ intermediate [25]. Absorbances at 1547 and 1528 cm⁻¹ can be assigned to NO species bound on V-W₁₈O₄₉ [26]. Then, two peaks at 1407 and 1349 cm⁻¹ are assigned to the NO₃ vibration and the peaks at 1259 cm⁻¹ can be attributed to asymmetric NO₂ bending, respectively [26,27]. These data suggest that adsorbed N₂ was more likely to be converted into *ON through an *O₂N₂ intermediate under light irradiation. In contrast, the in-situ DRIFTS spectra of the W₁₈O₄₉ nanowires under the same circumstances showed much weaker features, showing that the V doping is key aspect for the generation of the intermediate N-containing species, for the improved N₂ oxidation process.

3.3. Electronic and atomic structure

We have attempted to probe the electronic and atomic structure of V-W₁₈O₄₉ in order to provide an insight into the outstanding photocatalytic performance. X-ray photoelectron spectroscopy (XPS) experiments were conducted to investigate the surface composition and chemical states within V-W₁₈O₄₉ (Fig. S10). As shown in Fig. 3a, the W 4f photoemission features revealed that both W⁶⁺ (BE at 36.04 and 38.16 eV) and W⁵⁺ (BE at 34.64 and 37.03 eV) are present in W₁₈O₄₉ [28]. Significantly, the binding energy of the W 4f photoemission in V-W₁₈O₄₉ decreases by ~0.36 eV compared with pristine W₁₈O₄₉, confirming efficient intrinsic electronic coupling between the W and V species [8]. Furthermore, the three peaks of V 2p_{3/2} were located at 517.0, 516.2, and 515.1 eV, which could be denoted as V³⁺, V⁴⁺, and V⁵⁺, respectively, indicating that V³⁺ was partially oxidized to V⁴⁺ or V⁵⁺ during the synthetic process (Fig. S11) [29,30]. As shown in Fig. 3b, the O 1s photoemission for W₁₈O₄₉ can be assigned to lattice oxygen (~530.5 eV, O_{lat}), oxygen defect (~531.7 eV, O_{def}) and adsorbed oxygen (~533.0 eV, O_{ads}), respectively [31]. Both W₁₈O₄₉ and V-W₁₈O₄₉ nanowires exhibited an almost equivalent intensity O 1s photoemission, which implies that V substitutes for W at surface defect sites rather than

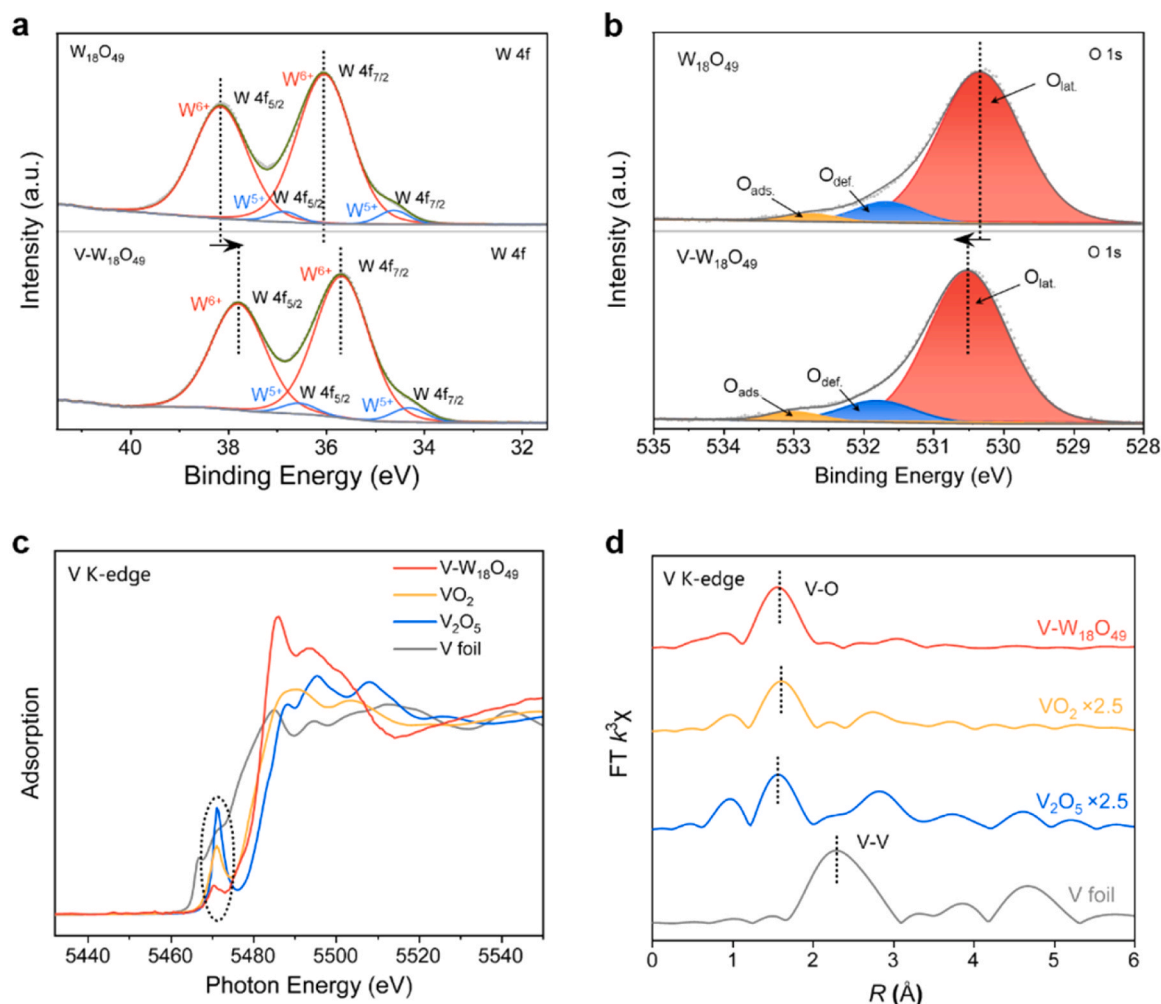


Fig. 3. The high-resolution XPS spectra of (a) W 4f and (b) O1s XPS spectra for $W_{18}O_{49}$ and $V-W_{18}O_{49}$. (c) V K-edge XANES spectra and (d) V K-edge FT-EXAFS data for $V-W_{18}O_{49}$ and selected V-containing reference materials.

creating new defects [10]. X-ray absorption spectroscopy (XAS) measurements are also in agreement with this hypothesis. For $V-W_{18}O_{49}$, the W L₃-edge X-ray absorption near-edge structure (XANES) spectra (Fig. S12a) indicated a decrease of the unoccupied electron density states at the W sites, confirming a higher electron density on the W atoms [22]. This distinct change in electron density of on the W atoms is controlled by the V doping [32]. The corresponding Fourier-transformed extended X-ray absorption fine structure (EXAFS) spectra (Fig. S12b) showed that V doping does not alter the W-O bonds lengths in the first coordination shell. There is no indication of a lowering to the coordination number around W as the result of the creation of oxygen defects in $V-W_{18}O_{49}$, which was in accordance with the XPS results [10]. V K-edge XAS was used to investigate the coordination environment of the doped V. In the V K-edge XANES spectra (Fig. 3c), the pre-edge feature indicated the V centers were coordinative unsaturated [33]. The corresponding V K-edge EXAFS spectra (Fig. 3d) showed a V-O shell at 1.51 \AA , which nearly overlays with the V-O shell at 1.53 \AA (VO_2) and 1.47 \AA (V_2O_5) [34]. Compared with V foil, $V-W_{18}O_{49}$ showed no features corresponding to V-V/V-O-V bonding, indicating no aggregation and the formation of V/VO_x particles or clusters upon V doping. To further resolve the location of V in $V-W_{18}O_{49}$, we conducted quantitative EXAFS fitting (Fig. S13, parameters were listed in Supplementary Table 4). Refinement of the EXAFS data, produces an average 1st shell V coordination number of 4.62 with the bond length of 1.98 \AA . The EXAFS fitting is also consisted with V substitution for W, and it is proved by the favorable formation energy calculations for V-doped slab models

(Fig. S15, Supplementary Table 5).

3.4. Electronic structure studies

To explore the origin of the high activity for nitrate production over $V-W_{18}O_{49}$, the effect of V doping on electronic structure was investigated. The UV-vis spectrum of $W_{18}O_{49}$ and $V-W_{18}O_{49}$ showed absorption edges at 426 and 397 nm (2.90 eV for $W_{18}O_{49}$, 2.98 eV for $V-W_{18}O_{49}$, Fig. 4a), where the larger band gaps of $V-W_{18}O_{49}$ could weaken energy relaxation for the electron-hole recombination. Correspondingly, the doping of V in $W_{18}O_{49}$ significantly upshift the defect band (DB) center toward the E_f (0.89 eV for $W_{18}O_{49}$, 0.66 eV for $V-W_{18}O_{49}$, Fig. S15), which may result in a large overlap between DB and CB of $V-W_{18}O_{49}$, weakening energy relaxation and reducing charge recombination. Combining the work function (Φ) (3.54 eV for $W_{18}O_{49}$, 3.46 eV for $V-W_{18}O_{49}$, Fig. S16), we obtained the corresponding band-edge positions of $V-W_{18}O_{49}$ (vs. NHE, Fig. S17), which satisfies the energy requirement of N_2 oxidation from thermal dynamic view.

The intrinsic electron transfer properties of catalyst is crucial in determining the kinetics of photocatalytic NOR. We have used ultrafast transient absorption (TA) spectroscopy to track the charge carrier dynamics in the photocatalysts in a real-time [35]. In our TA measurements, 360 and 800 nm pump pulses were chosen to facilitate electrons from the valence band (VB) to conduction band (CB). The spectra recorded following 360 and 800 nm pump pulses were significant different (Fig. 4b-f, Fig. S18), which probably originated from the

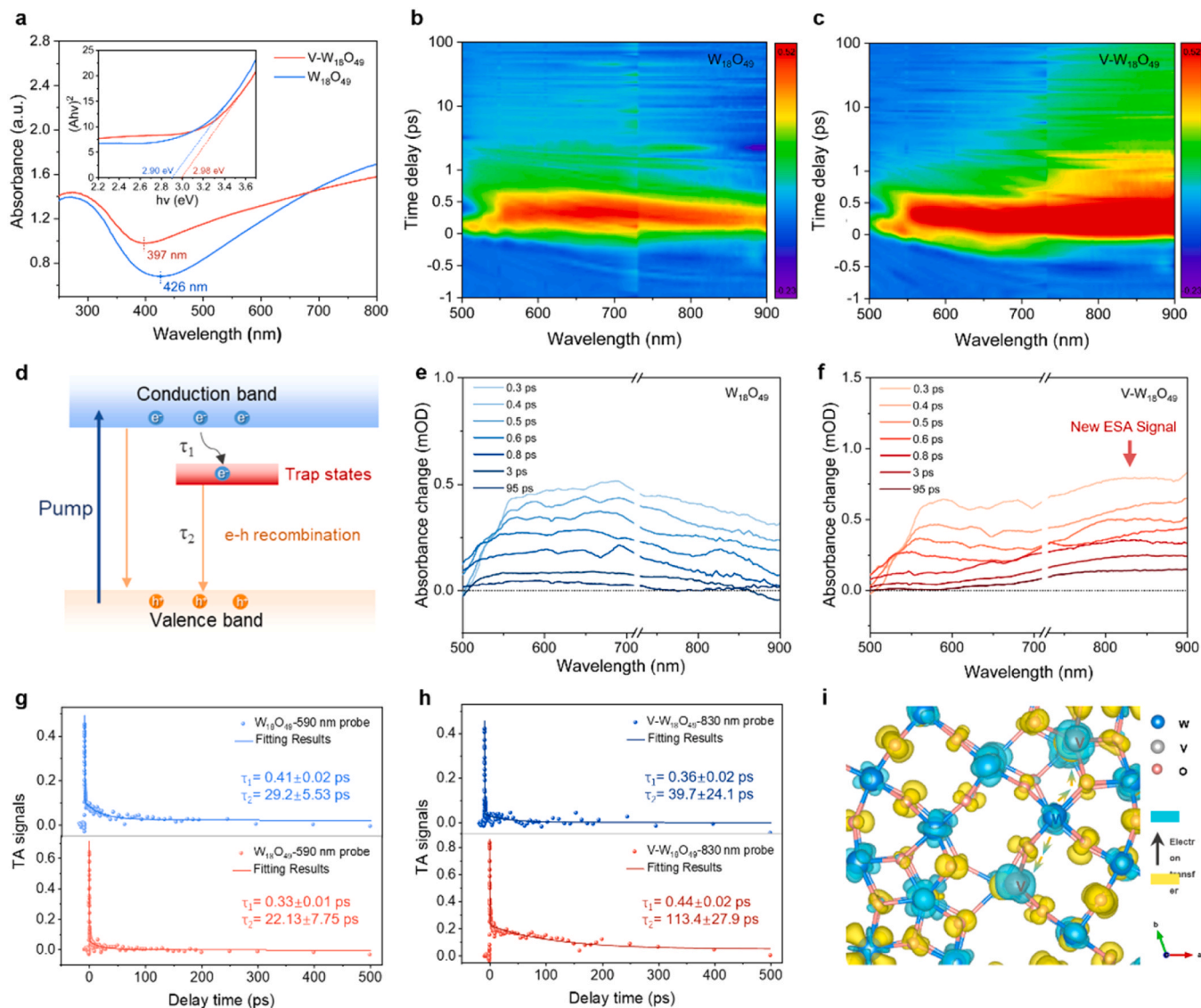


Fig. 4. (a) The UV-vis absorbance spectroscopy and Tauc plots (inset) for $W_{18}O_{49}$ and $V-W_{18}O_{49}$. Two-dimensional pseudo-color maps of TA spectra of (b) $W_{18}O_{49}$ and (c) $V-W_{18}O_{49}$ at 360 nm laser excitation. (d) Schematic illustration of the relaxation processes. Ultrafast transient absorption (TA) spectroscopy spectra at several probe delays for (e) $W_{18}O_{49}$, and (f) $V-W_{18}O_{49}$ at 360 nm laser excitation. The wavelength of 710–730 nm attributed to pump scattering. The TA spectroscopy kinetic traces of pristine (g) $W_{18}O_{49}$ and (h) $V-W_{18}O_{49}$ nanowires (probing wavelength at 590 and 830 nm, respectively). (i) The charge density difference of $V-W_{18}O_{49}$ under excited states (excitation wavelength at 318 nm).

different excited transient species. Combined the AQE data, we chose the spectra of 360 nm excitation to explore the photo-induced electron transfer process (Fig. 4d). As shown in Fig. 4e-f, the positive absorption spectra in the range of 500 ~ 900 nm belonged to the excited state absorption (ESA), which were assigned to the interactions between exciton bands [36]. In $W_{18}O_{49}$ sample, the ESA amplitude (750 ~ 900 nm) was significantly deactivated (Fig. 4b, 4e). In contrast, after V doping, the corresponding ESA signal of $V-W_{18}O_{49}$ was clearly enhanced as marked from 750 ~ 900 nm (Fig. 4c, 4f), decays more slowly and totally different from that in the spectra range of 500 ~ 750 nm, which indicated that the V-doping gives rise to a new photoinduced absorption signal in $V-W_{18}O_{49}$ structure, that may give significant insight into the electron-hole dynamics in $V-W_{18}O_{49}$ systems, a key aspect of driving nitrogen oxidation reactions, as discussed below.

Thus, we determined the photoinduced electron transfer time of $W_{18}O_{49}$ and $V-W_{18}O_{49}$ by fitting the decay kinetics with a biexponential function (Fig. 4g-h). Due to the different transient species, we chosen probing wavelengths of 590 and 830 nm, respectively. The relaxation

time implied that electron transfer from the CB minimum to trap states (τ_1) and recombination with the holes (τ_2), respectively [37]. As we attempted to study the charge dynamics, we specifically emphasized the longer relaxation (τ_2) when pumped at 360 nm for the interband transition. For the 590 nm probe wavelength (Fig. 4g), the decay time of $W_{18}O_{49}$ ($\tau_2 = 29.2$ ps) was slightly longer than $V-W_{18}O_{49}$ ($\tau_2 = 22.1$ ps). In contrast, for the 800 nm probe wavelength (Fig. 4h), the decay time of $V-W_{18}O_{49}$ was substantially lengthened to 113.4 ± 27.9 ps (τ_2), much longer than that of $W_{18}O_{49}$ ($\tau_2 = 39.7 \pm 24.1$ ps). This longer decay time ensured an effective charge separation and slows down electron transfer in the photocatalytic nitrogen fixation reaction [28]. Additionally, the enhanced photoinduced carrier separation and transformation in $V-W_{18}O_{49}$ can also be confirmed by transient photocurrent responses (Fig. S19a) and Nyquist plots of electrochemical impedance spectra (EIS, Fig. S19b). In summary, there was an additional electron transfer (ET) channel between the V-doped species and the W-O sites, which contributes to enhanced photocatalytic NOR kinetics as due to its longer electron decay time.

To further investigate the direction of electron transfer under illumination, time-dependent DFT (TDDFT) calculated absorption spectra [38] for $V-W_{18}O_{49}$ surfaces were collected, where the vertical lines denote the corresponding electron excitation energies and oscillator strengths, and the calculated absorption ability is much accordance to the experiment result (Fig. S20). Based on the isosurfaces of electron density differences (Fig. 4i), a visible electron transferring phenomenon from the W-O sites to the V center could be observed. And the peak value, oscillator strength and orbital contribution information corresponding to absorption peak are provided in Supplementary Table 6. Consequently, the reduced electron concentrations at the W sites may inhibit overly-strong adsorption of the reactant, and promoted the subsequent nitrogen activation.

3.5. DFT calculations

Recent studies have revealed that N_2 can be activated through the combination of σ -donation and π -back-donation effects [39,40]. The photocatalysts synchronously accept the unpaired electrons of N_2 and injected p electrons into the empty π^* orbitals of N_2 , consequently breaking the ultrastable $N\equiv N$ bond. Zhang *et al.* reported that superoxide species (*O_2) is one of the active intermediates in the photocatalytic NOR. And the $N\equiv N$ bond of the N_2 can be weakened by *O_2 and photo-induced electrons [25]. In this case, the O_2 can absorb at the metal sites and then accept photo-induced electrons to form superoxide species ($M-O_2^*$), which have appropriate energy and similar orbital symmetry to synergically accept electron density from and back-donate to N_2 [25,41]. In details, it could inject p electrons to the empty π^*

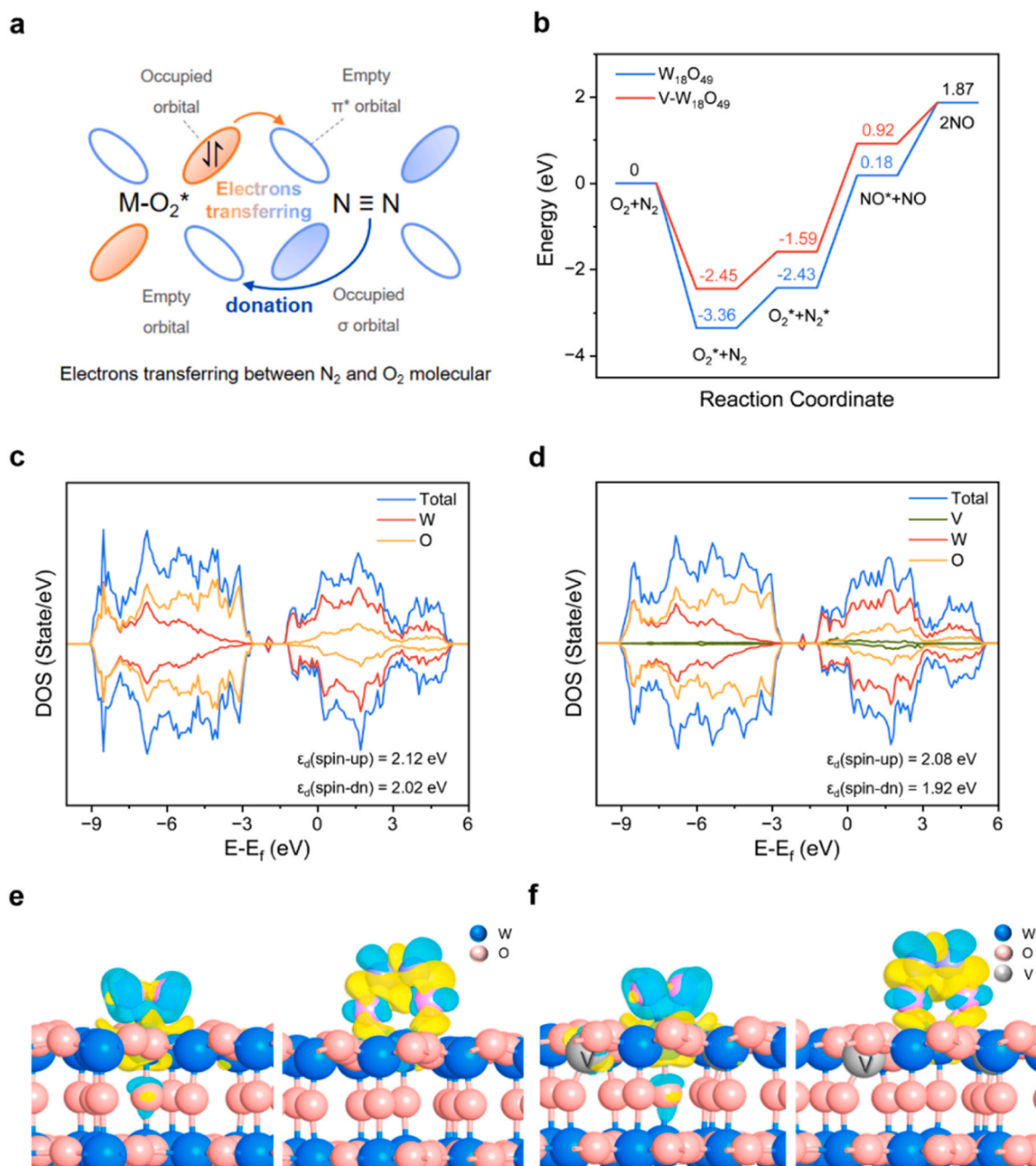


Fig. 5. (a) The scheme of electrons transferring between N_2 and O_2 molecular. (b) The energy profile of N_2 activation on $W_{18}O_{49}$ and $V-W_{18}O_{49}$ under excited states. The projected density of states (pDOS) of (c) $W_{18}O_{49}(010)$ and (d) $V-W_{18}O_{49}(010)$ surfaces. The fermi level was set to zero. The charge density difference of O_2 and N_2 adsorption on (e) $W_{18}O_{49}$ and (f) $V-W_{18}O_{49}$. The blue and yellow regions represent electron accumulated and deficient. The cutoff of isosurface is set to $0.001e/\text{Bohr}^3$.

orbitals of N_2 and accept electrons from the occupied σ orbital of N_2 , thereby weakening the $N\equiv N$ triple bonds.

To gain a deeper understanding of the photocatalytic NOR process, constrained density functional theory (DFT) calculations were employed to simulate the photooxidation of N_2 . Theoretically, it is widely accepted that the adsorbed N_2 (N_2^*) could preferentially convert into several adsorbates at high oxidation potentials, such as NO and the as-generated NO species will react with O_2 and ambient H_2O to form NO_3^- through a nonphotochemical step (a redox reaction at room temperature) [42,43]. Therefore, combined with the in-situ DRIFTS results, we mainly investigated the photochemical steps, for example, the conversion of N_2 into NO. The details of simulation models and calculation methodologies can be found in the Supplementary Note. According to the adsorption energy calculations of N_2 and O_2 on $W_{18}O_{49}$ surface, the interaction between substrate and O_2 is stronger than that between substrate and N_2 , suggesting that the O_2 is more preferable to adsorb on $W_{18}O_{49}$ surface in thermodynamics (Fig. S21–22). The calculated energy profile (Fig. 5b, Fig. S23–24) revealed that the adsorption energy of oxygen on the pristine $W_{18}O_{49}(010)$ surface was -3.36 eV. However, after replacing two surface W atoms with V, the adsorption energy of oxygen decreased to -2.45 eV, indicating that V doping can inhibit the strong adsorption strength of oxygen. With regard to N_2 adsorption, it prefers to interact with two atoms of adsorbed oxygen to form $O_2N_2^*$ intermediate, the adsorption energies were similar with and without V doping (0.93 eV vs. 0.86 eV). The rate-determining step for the dissociation of $O_2N_2^*$ to produce NO^* and gaseous NO was an endothermic process that required an energy input of 2.61 eV and 2.51 eV on $W_{18}O_{49}(010)$ and V- $W_{18}O_{49}(010)$ surfaces, respectively. In the case of NO desorption, the endothermal energy decreased from 1.69 eV to 0.95 eV after V doping in $W_{18}O_{49}$ surface. In summary, the N_2 could directly adsorb on the pre-adsorbed oxygen on V- $W_{18}O_{49}$ to form the metastable $*O_2N_2$ intermediates and dissociated into NO^* and gaseous NO. Then it further spontaneously translated into NO_2 and NO_3^- by O_2 and oxidative radicals in photocatalysis [25,44]. The unconverted NO and NO_2 can flow into water tank and react with O_2 and H_2O to produce HNO_3 as the final product [42,43].

To elucidate how the tuning of local electronic structure by V dopants, projected density of states (pDOS) calculation was carried out. It was showed that the shapes of the DOS were almost unchanged after V doping, but the d band center (ϵ_d) of W atoms shifted to a lower energy level (Fig. 5c–d) of 2.08 eV compared to 2.12 eV of $W_{18}O_{49}$. According to the d band model, a lower d band center indicates a weaker interaction between adsorbates and substrates. Therefore, the down-shifted d band of W atoms with V doping inhibited the over-strong adsorption of reactants on the surface. Based on the charge density difference calculations (Fig. 5e–f), it appeared that the O_2 gained electrons from the substrate, as evidenced by the accumulation of electron density around O_2 . Bader charge analysis revealed that the O_2 gained $0.92 e^-$ and $0.87 e^-$, while the N_2 lost $0.15 e^-$ and $0.16 e^-$ on the $W_{18}O_{49}$ and V- $W_{18}O_{49}$ surfaces, respectively (Supplementary Table 7). This indicated that V doping inhibited electron transfer from substrates to the O_2 , resulting in weaker adsorption of O_2 on the V- $W_{18}O_{49}$ surface. However, for N_2 adsorption, V doping enhanced electron transfer from O_2 to N_2 , leading to improved N_2 activation. These DFT results revealed that the V doping significantly optimized local electron properties, thus inhibiting the over-strong adsorption of O_2 and promoting N_2 activation by enhanced the π -backdonation process, which was beneficial to photocatalytic N_2 oxidation. In summary, the V doping can regulate the local electron density, showing the reduction of electronic concentration at W sites, which can suppress the over-strong adsorption of O_2 and promote electron transferred to the empty π^* -orbitals of N_2 , to promote $N\equiv N$ bond cleavage.

3.6. Evaluation of V- $W_{18}O_{49}$ nanowires as catalyst for N-fertilizer

With the remarkable NOR performance of our optimum performing

V- $W_{18}O_{49}$ catalyst, we further connected the photocatalytic nitrogen fixation with a hydroponics system with the goal of directly supplying N-fertilizer for the plant growth. Fig. 6a describes a system consisting of a handmade quartz reactor containing a V- $W_{18}O_{49}$ catalyst and an artificial climate chamber for vegetable cultivation (more details are provided in the Methods and Table S8). We started comparable Cole seeds in a 2 days germination timer, then transferred them into N-free solution-filled growing pots three days later (Fig. S25, Fig. S26a). The identical young seedlings were then transferred for further cultivation to three nutrition solutions with varying nitrogen concentrations: standard control group (standard Hoagland's solution [45]), blank control group (non-nitrogenous Hoagland's solution), and experimental group (solar nitrate fertilizer solution). The accumulated photocatalytic product was added into the growing pot to act as initial N-fertilizer for the experimental group, and subsequently the photocatalytic products were added each day to artificially mimic the solar energy driven fertilizer supplement. As can be seen from Fig. 6b–d and Fig. S26b, after two weeks growth, there was no obvious difference in Cole growth between the experimental and standard control groups: in fact, both groups had larger, greener leaves. In contrast, for the blank control group that without N-fertilizer, the Cole suffered from yellowing leaves and stagnant growth because of the absence of N-fertilizer during the growth process. Furthermore, we detected the nitrate content changes of nutrient solution along with the hydroponic Cole growth (Fig. 6e). Compared with the standard control group, solar nitrate addition in the experimental group resulted in lower starting nitrate concentration and smaller fluctuations of nitrate concentration. The particular solar-driven nitrate content modifications in the experimental group may prevent excessive nitrogen losses at an earlier stage and provide appropriate N-fertilizer when the crop needs it [46].

Moreover, to quantitatively analyze the effect of solar nitrate N-fertilizer on Cole growth, we detected the dry weight and total N content. Under simulated solar irradiation, there was no significant difference in dry weight and total N content (Fig. 6f) between the experimental group and standard control group. The aforementioned findings demonstrated the viability of the photocatalytic nitrogen fixation system to provide N-fertilizer for the Cole to absorb effectively during their growth process. The total N (Fig. 6f) and nitrogen usage efficiency (NUE; Fig. 6g) for the experimental group were 2.47 mg and 63.82% , respectively, both were comparable to those of the control group (2.01 mg in total N and 54.08% in NUE, respectively). The solar N-fertilizer lead to Low-nitrogen stress in the initial phase and increased dissolved oxygen (DO) in Cole growth system, which may account for the higher performance of the experimental group [47,48]. The photocatalyst that after cultivation experiment was characterized by XRD (Fig. S26). The V- $W_{18}O_{49}$ showed structural stability that can be maintained after the vegetable cultivation, which proved that the photocatalyst has good stability in solar N-fertilizer synthesis. In this study, we demonstrated a solar-driven photocatalytic process utilizing the V- $W_{18}O_{49}$ catalyst to convert atmospheric nitrogen into N-fertilizer, resulting in an improved plant growth. Our findings indicate that the efficacy of this process is comparable to that of commercially available nutrient solutions during the seedling stage. Solar-based nitrogen fertilizers are considered to be a cost-effective and environmentally sustainable alternative, as their primary source from air and solar energy.

4. Conclusions

In conclusion, the as-activated V- $W_{18}O_{49}$ exhibiting a high photocatalytic activity for nitrate synthesis. Under light irradiation, the production rate of nitrate is $39.85 \mu\text{mol g}^{-1} \text{h}^{-1}$ with close to 100% selectivity. The improved photocatalytic N_2 oxidation activities were largely attributable to the optimized electronic structures, which result in a new high-efficiency electron transfer channels from W-O sites to V-dopant and facilitated the formation of $*ON$ and NO desorption with accelerated electron-transfer kinetics. More interesting, the V-doped

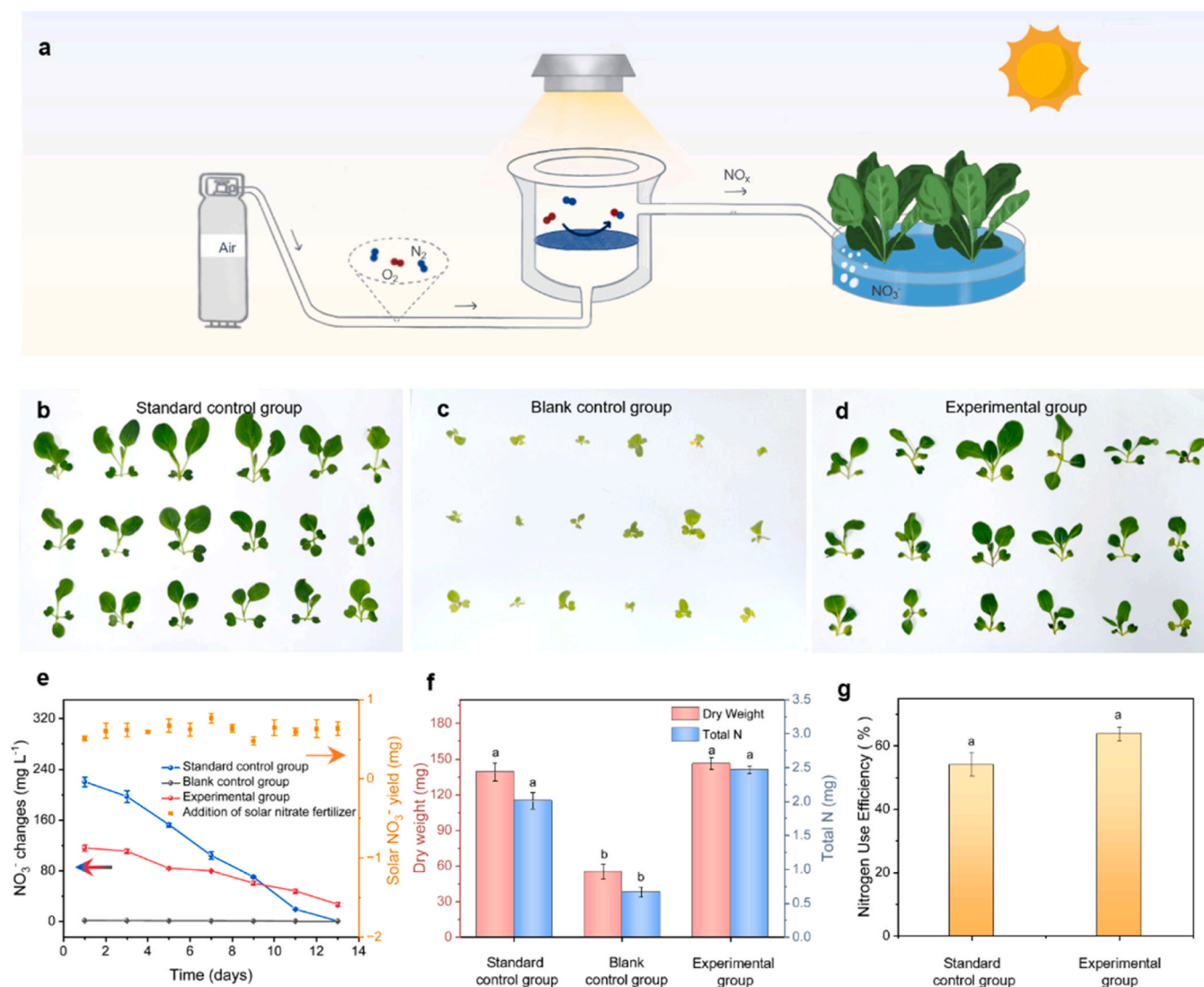


Fig. 6. (a) Scheme 1. V-W₁₈O₄₉ are activated by simulated solar light, producing nitrate fertilizer for vegetable cultivation. (b) Standard control group (standard Hoagland's solution). (c) Blank control group (non-nitrogenous Hoagland's solution), and (d) Experimental group (solar nitrate fertilizer solution). (e) The nitrate content changes of nutrient solution in artificial climate chamber hydroponic Cole and the NO₃⁻ N-fertilizer added to the experimental group that generated by photocatalytic reactions under AM 1.5 G irradiation (50 mg V-W₁₈O₄₉ as the photocatalyst and 16 h for one day). (f) The dry weight and total N in Cole. (g) The nitrogen use efficiency in experiment and control groups. Data represent means ± s.d. and the different letters represent significant differences (P < 0.05 by one-way ANOVA with Tukey's post-hoc test).

W₁₈O₄₉ nanowires was used for the on-site, on-demand direct synthesis of nitrate fertilizers for enhanced leafy crop growth. This study provides fresh insights into the rational design of highly effective photocatalysts for the synthesis of solar-derived nitrate fertilizer.

CRediT authorship contribution statement

Shaoquan Li synthesized the catalyst, conducted the photocatalytic nitrogen oxidation reaction experiments, performed all the characterization analysis. Jinjia Liu performed the DFT calculations and Xiaodong Wen contributed to the discussion on the DFT calculations. Wenli Su, Wenkai Zhang were helpful in the fs-TA analysis. Yi Wang performed the TDDFT calculations. Jinhao Li and Chenjun Ning repeated the photocatalytic experiment to ensure that the experimental results are reproducible. Jing Ren were helpful in the XAFS analysis and optimization of reaction conditions. Yuxin Tong, Chong Wang assisted with the crop hydroponics system. Lirong Zheng helped supervise the XAFS analysis. Xue Duan, YuFei Zhao designed the study, supervised all the experiments. Dermot O'Hare, Wei Zhang assisted in the drafting

and review of the manuscript.

Declaration of Competing Interest

The authors declare that they have no known competing financial interests or personal relationships that could have appeared to influence the work reported in this paper.

Data availability

Data will be made available on request.

Acknowledgements

This research was supported by National Natural Science Foundation of China (22278030, 22090032, 22090030, 22288102, 22011530162, 22202224). The XAFS experiments were conducted in 1W1B beamline of the Beijing Synchrotron Radiation Facility.

Appendix A. Supporting information

Supplementary data associated with this article can be found in the online version at [doi:10.1016/j.apcatb.2023.123539](https://doi.org/10.1016/j.apcatb.2023.123539).

References

- [1] X. Zhang, X. Zhu, S. Bo, C. Chen, M. Qiu, X. Wei, N. He, C. Xie, W. Chen, J. Zheng, P. Chen, S.P. Jiang, Y. Li, Q. Liu, S. Wang, Identifying and tailoring C-N coupling site for efficient urea synthesis over diatomic Fe-Ni catalyst, *Nat. Commun.* 13 (2022), 5337, <https://doi.org/10.1038/s41467-022-33066-6>.
- [2] R. Shi, X. Zhang, G.L.N. Waterhouse, Y. Zhao, T. Zhang, The journey toward low temperature, low pressure catalytic nitrogen fixation, *Adv. Energy Mater.* 10 (2020), 2000659, <https://doi.org/10.1002/aenm.202000659>.
- [3] S. Liu, Z. Teng, H. Liu, T. Wang, G. Wang, Q. Xu, X. Zhang, M. Jiang, C. Wang, W. Huang, H. Pang, A Ce-Uio-66 metal-organic framework-based graphene-embedded photocatalyst with controllable activation for solar ammonia fertilizer production, *Angew. Chem. Int. Ed.* 61 (2022), e202207026, <https://doi.org/10.1002/anie.202207026>.
- [4] L. Huang, L. Cheng, T. Ma, J.J. Zhang, H. Wu, J. Su, Y. Song, H. Zhu, Q. Liu, M. Zhu, Z. Zeng, Q. He, M.K. Tse, D.T. Yang, B.I. Yakobson, B.Z. Tang, Y. Ren, R. Ye, Direct synthesis of ammonia from nitrate on amorphous graphene with near 100% efficiency, *Adv. Mater.* (2023), 2211856, <https://doi.org/10.1002/adma.202211856>.
- [5] S.-J. Yuan, J.-J. Chen, Z.-Q. Lin, W.-W. Li, G.-P. Sheng, H.-Q. Yu, Nitrate formation from atmospheric nitrogen and oxygen photocatalysed by nano-sized titanium dioxide, *Nat. Commun.* 4 (2013), 2249, <https://doi.org/10.1038/ncomms3249>.
- [6] J. Yang, H. Bai, Y. Guo, H. Zhang, R. Jiang, B. Yang, J. Wang, J.C. Yu, Photodriven disproportionation of nitrogen and its change to reductive nitrogen photofixation, *Angew. Chem. Int. Ed.* 60 (2021) 927–936, <https://doi.org/10.1002/anie.202010192>.
- [7] X. Liu, Y. Luo, C. Ling, Y. Shi, G. Zhan, H. Li, H. Gu, K. Wei, F. Guo, Z. Ai, L. Zhang, Rare earth La single atoms supported MoO₃-x for efficient photocatalytic nitrogen fixation, *Appl. Catal. B: Environ.* 301 (2022), 120766, <https://doi.org/10.1016/j.apcatb.2021.120766>.
- [8] H. Zhang, Y. Wang, S. Zuo, W. Zhou, J. Zhang, X.W.D. Lou, Isolated cobalt centers on W₁₈O₄₉ nanowires perform as a reaction switch for efficient CO₂ photoreduction, *J. Am. Chem. Soc.* 143 (2021) 2173–2177, <https://doi.org/10.1021/jacs.0c08409>.
- [9] Z. Ying, S. Chen, S. Zhang, T. Peng, R. Li, Efficiently enhanced N₂ photofixation performance of sea-urchin-like W₁₈O₄₉ microspheres with Mn-doping, *Appl. Catal. B: Environ.* 254 (2019) 351–359, <https://doi.org/10.1016/j.apcatb.2019.05.005>.
- [10] N. Zhang, A. Jalil, D. Wu, S. Chen, Y. Liu, C. Gao, W. Ye, Z. Qi, H. Ju, C. Wang, X. Wu, L. Song, J. Zhu, Y. Xiong, Refining defect states in W₁₈O₄₉ by Mo doping: a strategy for tuning N₂ activation towards solar-driven nitrogen fixation, *J. Am. Chem. Soc.* 140 (2018) 9434–9443, <https://doi.org/10.1021/jacs.8b02076>.
- [11] G. Dong, X. Huang, Y. Bi, Anchoring black phosphorus quantum dots on Fe-doped W₁₈O₄₉ nanowires for efficient photocatalytic nitrogen fixation, *Angew. Chem. Int. Ed.* 61 (2022), e202204271, <https://doi.org/10.1002/anie.202204271>.
- [12] P. Xia, X. Pan, S. Jiang, J. Yu, B. He, P.M. Ismail, J.Y. Wei Bai, L. Yang, H. Zhang, M. Cheng, H. Li, Q. Zhang, C. Xiao, Y. Xie, Designing a redox heterojunction for photocatalytic “overall nitrogen fixation” under mild conditions, *Adv. Mater.* 34 (2022), 2200563, <https://doi.org/10.1002/adma.202200563>.
- [13] Y. Zhao, Y. Zhao, G.L.N. Waterhouse, L. Zheng, X. Cao, F. Teng, L.-Z. Wu, C.-H. Tung, D. O'Hare, T. Zhang, Layered-double-hydroxide nanosheets as efficient visible-light-driven photocatalysts for dinitrogen fixation, *Adv. Mater.* 29 (2017), 1703828, <https://doi.org/10.1002/adma.201703828>.
- [14] R. Fu, Z. Wu, Z. Pan, Z. Gao, Z. Li, X. Kong, L. Li, Fluorine-induced surface metallization for ammonia synthesis under photoexcitation up to 1550 nm, *Angew. Chem. Int. Ed.* 60 (2021) 11173–11179, <https://doi.org/10.1002/anie.202100572>.
- [15] S. Sun, X. Li, W. Wang, L. Zhang, X. Sun, Photocatalytic robust solar energy reduction of dinitrogen to ammonia on ultrathin MoS₂, *Appl. Catal. B: Environ.* 200 (2017) 323–329, <https://doi.org/10.1016/j.apcatb.2016.07.025>.
- [16] G. Kresse, J. Furthmüller, Efficiency of ab-initio total energy calculations for metals and semiconductors using a plane-wave basis set, *Comp. Mater. Sci.* 6 (1996) 15–50, [https://doi.org/10.1016/0927-0256\(96\)00008-0](https://doi.org/10.1016/0927-0256(96)00008-0).
- [17] P. Blöchl, Projector augmented-wave method, *Phys. Rev. B* 50 (1994) 17953–17979, <https://doi.org/10.1103/physrevb.50.17953>.
- [18] G. Kresse, D. Joubert, From ultrasoft pseudopotentials to the projector augmented-wave method, *Phys. Rev. B* 59 (1999) 1758–1775, <https://doi.org/10.1103/PhysRevB.59.1758>.
- [19] J.P. Perdew, K. Burke, M. Ernzerhof, Generalized gradient approximation made simple, *Phys. Rev. Lett.* 77 (1996) 3865–3868, <https://doi.org/10.1103/PhysRevLett.77.3865>.
- [20] B. Kaduk, T. Kowalczyk, T. Van Voorhis, Constrained density functional theory, *Chem. Rev.* 112 (2012) 321–370, <https://doi.org/10.1021/cr200148b>.
- [21] T.D. Kühne, M. Iannuzzi, M. Del Ben, V.V. Rybkin, P. Seewald, F. Stein, T. Laino, R. Z. Khaliullin, O. Schütt, F. Schiffmann, CP2K: An electronic structure and molecular dynamics software package-Quickstep: efficient and accurate electronic structure calculations, *J. Chem. Phys.* 152 (2020), 194103, <https://doi.org/10.1063/1.5000705>.
- [22] G. Xi, S. Ouyang, P. Li, J. Ye, Q. Ma, N. Su, H. Bai, C. Wang, Ultrathin W₁₈O₄₉ nanowires with diameters below 1 nm synthesis, near-infrared absorption, photoluminescence, and photochemical reduction of carbon dioxide, *Angew. Chem. Int. Ed.* 51 (2012) 2395–2399, <https://doi.org/10.1002/anie.201107681>.
- [23] J. Jiang, F. Sun, S. Zhou, W. Hu, H. Zhang, J. Dong, Z. Jiang, J. Zhao, J. Li, W. Yan, M. Wang, Atomic-level insight into super-efficient electrocatalytic oxygen evolution on iron and vanadium co-doped nickel (oxy)hydroxide, *Nat. Commun.* 9 (2018), 2885, <https://doi.org/10.1038/s41467-018-05341-y>.
- [24] S. Han, C. Wang, Y. Wang, Y. Yu, B. Zhang, Electrosynthesis of nitrate via the oxidation of nitrogen on tensile-strained palladium porous nanosheets, *Angew. Chem. Int. Ed.* 60 (2021) 4474–4478, <https://doi.org/10.1002/anie.202014017>.
- [25] S. Zhang, Y. Zhao, Y. Miao, Y. Xu, J. Ran, Z. Wang, Y. Weng, T. Zhang, Understanding aerobic nitrogen photooxidation on titania through in situ time-resolved spectroscopy, *Angew. Chem. Int. Ed.* 61 (2022), e202211469, <https://doi.org/10.1002/anie.202211469>.
- [26] T. Li, S. Han, C. Cheng, Y. Wang, X. Du, Y. Yu, B. Zhang, Sulfate-enabled nitrate synthesis from nitrogen electrooxidation on a rhodium electrocatalyst, *Angew. Chem. Int. Ed.* 61 (2022), e202204541, <https://doi.org/10.1002/anie.202204541>.
- [27] J. Yang, L. Li, C. Xiao, Y. Xie, Dual-plasmon resonance coupling promoting directional photosynthesis of nitrate from air, *Angew. Chem. Int. Ed.* (2023), e202311911, <https://doi.org/10.1002/anie.202311911>.
- [28] J. Yang, Z. Ruan, S. Jiang, P. Xia, Q. Yang, Q. Zhang, C. Xiao, Y. Xie, Ce-doped W₁₈O₄₉ nanowires for tuning N₂ activation toward direct nitrate photosynthesis, *J. Phys. Chem. Lett.* 12 (2021) 11295–11302, <https://doi.org/10.1021/acs.jpclett.1c03207>.
- [29] G. Li, Y. Xu, H. Pan, X. Xie, R. Chen, D. Wu, L. Wang, A bimetallic synergistic effect on the atomic scale of defect-enriched NiV-layered double hydroxide nanosheets for electrochemical phenol hydroxylation, *J. Mater. Chem. A* 10 (2022) 6748–6761, <https://doi.org/10.1039/d1ta09412b>.
- [30] K. Fan, H. Chen, Y. Ji, H. Huang, P.M. Claesson, Q. Daniel, B. Philippe, H. Rensmo, F. Li, Y. Luo, L. Sun, Nickel–vanadium monolayer double hydroxide for efficient electrochemical water oxidation, *Nat. Commun.* 7 (2016), <https://doi.org/10.1038/ncomms11981>.
- [31] Xa Dong, Z. Cui, X. Shi, P. Yan, Z. Wang, A.C. Co, F. Dong, Insights into dynamic surface bromide sites in Bi₄O₅Br₂ for sustainable N₂ photofixation, *Angew. Chem. Int. Ed.* 61 (2022), e202200937, <https://doi.org/10.1002/anie.202200937>.
- [32] Y. Liang, Y. Li, H. Wang, J. Zhou, J. Wang, T. Regier, H. Dai, Co₃O₄ nanocrystals on graphene as a synergistic catalyst for oxygen reduction reaction, *Nat. Mater.* 10 (2011) 780–786, <https://doi.org/10.1038/nmat3087>.
- [33] J. Wong, F.W. Lytle, R.P. Messmer, D.H. Maylotte, K-edge absorption spectra of selected vanadium compounds, *Phys. Rev. B* 30 (1984) 5596–5610, <https://doi.org/10.1103/PhysRevB.30.5596>.
- [34] J. Liu, Y. Ji, J. Nai, X. Niu, Y. Luo, L. Guo, S. Yang, Ultrathin amorphous cobalt–vanadium hydroxide catalysts for the oxygen evolution reaction, *Energy Environ. Sci.* 11 (2018) 1736, <https://doi.org/10.1039/C8EE00611C>.
- [35] X. Zhang, X. Wu, X. Liu, G. Chen, Y. Wang, J. Bao, X. Xu, X. Liu, Q. Zhang, K. Yu, W. Wei, J. Liu, J. Xu, H. Jiang, P. Wang, X. Wang, Heterostructural CsPbX₃-PbS (X = Cl, Br, I) quantum dots with tunable Vis-NIR dual emission, *J. Am. Chem. Soc.* 142 (2020) 4464–4471, <https://doi.org/10.1021/jacs.9b13681>.
- [36] Z.H. Yan, M.H. Du, J. Liu, S. Jin, C. Wang, G.L. Zhuang, X.J. Kong, L.S. Long, L. S. Zheng, Photo-generated dinuclear {Eu(II)}₂ active sites for selective CO₂ reduction in a photosensitizing metal-organic framework, *Nat. Commun.* 9 (2018), 3353, <https://doi.org/10.1038/s41467-018-05659-7>.
- [37] H. Huang, L. Zhang, Z. Lv, R. Long, C. Zhang, Y. Lin, K. Wei, C. Wang, L. Chen, Z. Y. Li, Q. Zhang, Y. Luo, Y. Xiong, Unraveling surface plasmon decay in core-shell nanostructures toward broadband light-driven catalytic organic synthesis, *J. Am. Chem. Soc.* 138 (2016) 6822–6828, <https://doi.org/10.1021/jacs.6b02532>.
- [38] Z. Liu, T. Lu, Q. Chen, An sp-hybridized all-carboatomic ring, cyclo[18]carbon: bonding character, electron delocalization, and aromaticity, *Carbon* 165 (2020) 468–475, <https://doi.org/10.1016/j.carbon.2020.04.099>.
- [39] Z. Li, Z. Pan, S. Cai, Z. Gao, Z. Li, R. Fu, Z. Zhao, X. Mu, L. Li, Electronic and interface regulation of wurtzite surfaces promotes photocatalytic ammonia synthesis under visible light irradiation, *ACS Sustainable Chem. Eng.* 9 (2021) 13630–13639, <https://doi.org/10.1021/acscuschemeng.1c05107>.
- [40] Q. Han, C. Wu, H. Jiao, R. Xu, Y. Wang, J. Xie, Q. Guo, J. Tang, Rational design of high-concentration Ti³⁺ in porous carbon-doped TiO₂ nanosheets for efficient photocatalytic ammonia synthesis, *Adv. Mater.* 33 (2021), e2008180, <https://doi.org/10.1002/adma.202008180>.
- [41] M.-A. L  gar  , G. B  langer-Chabot, R.D. Dewhurst, E. Welz, I. Krummenacher, B. Engels, H. Braunschweig, Nitrogen fixation and reduction at boron, *Science* 359 (2018) 896–900, <https://doi.org/10.1126/science.aag1684>.
- [42] Y. Yu, C. Wang, Y. Yu, Y. Huang, C. Liu, S. Lu, B. Zhang, A nitrogen fixation strategy to synthesize NO via the thermally-assisted photocatalytic conversion of air, *J. Mater. Chem. A* 8 (2020) 19623–19630, <https://doi.org/10.1039/D0TA06747D>.
- [43] X. Zhang, R. Shi, Z. Li, J. Zhao, H. Huang, C. Zhou, T. Zhang, Photothermal-assisted photocatalytic nitrogen oxidation to nitric acid on palladium-decorated titanium oxide, *Adv. Energy Mater.* (2022), 2103740, <https://doi.org/10.1002/aenm.202103740>.
- [44] H. Li, H. Shang, X. Cao, Z. Yang, Z. Ai, L. Zhang, Oxygen vacancies mediated complete visible light NO oxidation via side-on bridging superoxide radicals, *Environ. Sci. Technol.* 52 (2018) 8659–8665, <https://doi.org/10.1021/acs.est.8b01849>.
- [45] L. Chekili, J.E. Kim, I. El Saliby, Y. Kim, S. Phuntsho, S. Li, N. Ghaffour, T. Leiknes, H. Kyong Shon, Fertilizer drawn forward osmosis process for sustainable water reuse to grow hydroponic lettuce using commercial nutrient solution, *Sep. Purif. Technol.* 181 (2017) 18–28, <https://doi.org/10.1016/j.seppur.2017.03.008>.

- [46] F. Teia, S.D. Neveb, Jd Haanc, H.L. Kristensen, Nitrogen management of vegetable crops, *Agr. Water Manag.* 240 (2020), 106316, <https://doi.org/10.1016/j.agwat.2020.106316>.
- [47] Z. Wu, J. Luo, Y. Han, Y. Hua, C. Guan, Z. Zhang, Low nitrogen enhances nitrogen use efficiency by triggering NO_3 uptake and its long-distance translocation, *J. Agric. Food Chem.* 67 (2019) 6736–6747, <https://doi.org/10.1021/acs.jafc.9b02491>.
- [48] S. Bonachela, J. Quesada, R.A. Acuña, J.J. Magañ, O. Marfa, Oxyfertilization of a greenhouse tomato crop grown on rockwool slabs and irrigated with treated wastewater: oxygen content dynamics and crop response, *Agr. Water Manag.* 97 (2010) 433–438, <https://doi.org/10.1016/j.agwat.2009.10.016>.